The Astrophysical Journal, 908:161 (7pp), 2021 February 20 https://doi.org/10.3847/1538-4357/abda40

Constraining the Metallicities of Damped Lyα Systems Using Extinction Curves

Hassan Fathivavsari
School of Astronomy, Institute for Research in Fundamental Sciences (IPM), P.O. Box 19395-5531, Tehran, Iran; h.fathie@gmail.com
Received 2020 October 9; revised 2021 January 5; accepted 2021 January 7; published 2021 February 22

Abstract

In this paper, we present a new method to constrain the metallicities of high-redshift damped Lyα (DLA) absorbers using observed extinction curves. This is the first time such an approach is employed to constrain the metallicities of extragalactic absorbers. To demonstrate our method, we use the spectra of 13 quasars and one gamma-ray burst (GRB) with DLA absorbers detected along their sightlines. By using the Kramers–Kronig (KK) relation, which relates the wavelength-integrated extinction to the total volume occupied by dust per hydrogen nucleon, we set some robust lower limits on the metallicity of the DLAs. The resulting lower limits are all consistent with the DLA metallicities from the literature. The GRB extinction curve exhibits a very strong 2175 Å extinction bump. We try to constrain the metallicity of the GRB DLA by modeling the GRB extinction curve using dust models with two (graphite and silicates) and three (polycyclic aromatic hydrocarbon, hydrogenated amorphous carbon, and silicates) dust components. The two-component model results in a metallicity of $Z\sim -0.45$, while the three-component model gives $Z\sim -0.50$. However, the lower limit from the KK approach for this DLA is $Z\geqslant -0.60$. Modeling a large sample of extinction curves with a 2175 Å extinction bump and measured DLA metallicities would allow a thorough comparison between the KK and the model-dependent approach. In cases where the precise measurement of the metallicity of a DLA is not possible (e.g., due to the saturation of important absorption lines), the approach presented in this paper can be used to constrain the metallicity.

Unified Astronomy Thesaurus concepts: Extinction (505); Ultraviolet extinction (1738); Galaxies (573); Gamma-ray bursts (629); Quasar absorption line spectroscopy (1317)

1. Introduction

The interstellar medium (ISM) of the Galaxy is composed of gas and dust. The gas-phase abundances of the elements present in the ISM can be measured from the absorption lines they produce in the spectra of background stars (Spitzer & Jenkins 1975; Savage et al. 1992; Spitzer & Fitzpatrick 1995; Welty et al. 1997; Gudennavar et al. 2012). The dust-phase abundance of an element is derived by subtracting off its gas-phase abundance from a reference abundance (Sofia et al. 1994; Vladilo 1998; Voshchinnikov & Henning 2010; De Cia et al. 2013). The solar abundance (Anders & Grevesse 1989; Asplund et al. 2009) is usually taken as the reference abundance. However, the protosolar abundances augmented by Galactic chemical enrichment and the abundances of the unevolved early B stars are also adopted as the reference abundances (Mishra & Li 2015, 2017).

The presence of dust in the ISM also attenuates and extincts the light of background stars through absorption and scattering. The extinction (which is the sum of absorption and scattering) is wavelength dependent in such a way that photons with bluer wavelengths tend to be more extincted. Due to this tendency, the wavelength dependence of extinction is often referred to as *reddening*. The amount of dust responsible for the observed extinction can be estimated using the Kramers–Kronig (KK) relation (Purcell 1969). As shown in Li (2005), the KK relation relates the wavelength-integrated extinction to the total volume (per hydrogen nucleon) occupied by dust through

$$\int_0^\infty \frac{A_\lambda}{N_{\rm H}} d\lambda = 1.086\times 3\pi^2 F \frac{V_{\rm dust}}{\rm H}, \quad (1)$$

where $N_{\rm H}$ is the hydrogen column density and F is a dimensionless factor that is a function of the grain shape and the static (zero-frequency) dielectric constant ϵ_0 of the dust grain material. The value of F for different dust materials can be calculated using Equation (4) in Mishra & Li (2015). Since A_λ is only known for a limited range of wavelengths, in practice, the integral in Equation (1) is usually calculated over the wavelength range of 912 Å $\leqslant\lambda\leqslant$ 1000 μm, and the result is considered as a lower limit. For the diffuse ISM, the integral of $A_\lambda/N_{\rm H}$ over this wavelength range is 1.49×10^{-25} mag cm^{-3} H^{-1}. In principle, this contains the contributions from different species of dust materials such as silicates and carbonaceous grains.

It has been well recognized that silicate is a major component of the ISM dust (Kim et al. 1994; Li & Draine 2001a, 2001b; Weingartner & Draine 2001; Zonca et al. 2011; Mishra & Li 2015, 2017; Wang et al. 2015; Gao et al. 2020; Ma et al. 2020). The presence of silicate grains in the ISM is primarily revealed through the detection of the 9.7 μm Si−O stretching and 18 μm O−Si−O bending absorption features (Jaeger et al. 1994; Henning 2010). The smooth and featureless structures of these absorption features indicate that the silicate grains in the ISM are predominantly of amorphous composition (Li & Draine 2001b; Kemper et al. 2004; Li et al. 2008).

Are silicate grains alone sufficient to explain the observed extinction? If we assume that all Si, Mg, and Fe elements of solar abundances (Asplund et al. 2009) are locked up in silicate grains with a stoichiometric composition of $MgFeSiO_4$, the upper limit that we get for the total silicate volume per H nucleon is

$$V_{\rm sil}/H \approx (M_{\rm sil}/M_{\rm H})/\rho_{\rm sil}\times m_{\rm H} \approx 2.71\times 10^{-27}\,{\rm cm^3\,H^{-1}}, \quad (2)$$

where $M_{\rm sil}/M_{\rm H}$ is the silicate to hydrogen mass, $\rho_{\rm sil}$ is the mass density of silicate, and $m_{\rm H}=1.66\times 10^{-26}$ g is the mass of hydrogen atom. With $F\approx 0.7$ (see Mishra & Li 2015), the

wavelength-integrated extinction originating from the silicate component of the dust is at most $\sim 6.01 \times 10^{-26}$ mag cm^3 H^{-1}. This is not sufficient to explain the observed lower limit of 1.49×10^{-25} mag cm^{-3} H^{-1}. The inability of silicate dust to fully account for the observed extinction implies that there must be other dust components present in the ISM, with carbonaceous dust being the most favored one.

The presence of carbonaceous dust in the ISM is spectroscopically revealed through the 3.4 μm aliphatic C−H stretching absorption feature (Adamson et al. 1990; Pendleton & Allamandola 2002), and the *unidentified* infrared emission bands at 3.3, 6.2, 7.7, 8.6, 11.3, and 12.7 μm (Leger & Puget 1984; Allamandola et al. 1985). The 2175 Å extinction bump is also widely attributed to the presence of small graphite grains (Stecher & Donn 1965; Draine & Malhotra 1993; Papoular & Papoular 2009), or polycyclic aromatic hydrocarbon (PAH) molecules (Li & Draine 2001b; Steglich et al. 2010; Xiang et al. 2011; Mulas et al. 2013; Bekki et al. 2015). The bump, which is the strongest absorption feature observed in the ISM, is thought to arise from the π–π^* transition in the sp^2 hybridization of aromatic carbon. As outlined above, the carbonaceous dust must account for more than half of the total observed extinction. Indeed, all modern extinction models assume that the observed extinction is predominantly caused by the combination of carbonaceous and silicate grains of various sizes (Draine & Lee 1984; Laor & Draine 1993; Kim et al. 1994; Weingartner & Draine 2001; Li & Draine 2001a, 2001b; Liang & Li 2009, 2010; Mishra & Li 2015, 2017; Wang et al. 2015; Ma et al. 2020).

In this paper, we introduce a method to derive some lower limits for the metallicity of high-redshift damped Lyα systems (DLAs) using the observed extinction curves. We demonstrate our method by applying it to the spectra of 13 quasars and one gamma-ray burst (GRB) along which some DLA absorbers are identified. Here, we take two different approaches: the first approach, which is independent of any dust model, is to use the Kramers–Kronig (KK) relation of Purcell (1969), and the second approach is to model the observed extinction curve in terms of two- and three-component dust models. These techniques can be used as a complement to the metal absorption line technique, especially in cases where the precise metallicity is not available. This is best suited for absorbers associated with GRBs, due to their simple spectral energy distributions that lack prominent emission lines (Zafar et al. 2011, 2012, 2018a, 2018b), and quasar absorbers with $z_{\rm DLA} \sim z_{\rm QSO}$, such as eclipsing and ghostly DLAs (Fathivavsari et al. 2015, 2016, 2017, 2018; Fathivavsari 2020a, 2020b). In the latter systems, the similarity of the absorption and emission redshift reduces the complications that may arise due to the presence of emission lines intrinsic to the quasar.

2. The Data

In this paper, we use the spectra of 13 quasars and one GRB to demonstrate our method. These quasars are selected for two reasons: (1) they all have a DLA at $z_{\rm abs} \sim z_{\rm em}$, and (2) the metallicities of their DLAs, which are measured from high-resolution spectra, are available in the literature. Table 1 summarizes the quasar redshift ($z_{\rm em}$), the DLA redshift ($z_{\rm abs}$), and the neutral hydrogen column density of the DLA (N(H I)), along with the references from which they are compiled. The similarity of the DLA absorption and quasar emission redshifts allows for a more accurate extraction of the extinction curve from the quasar spectra. None of these quasars exhibits the 2175 Å extinction bump. However, a strong 2175 Å bump is detected in the GRB spectrum. The bump is detected at the redshift of a DLA absorber with $z_{\rm abs} = 2.2486$ and a neutral hydrogen column density of $\log N({\rm H\,I/cm^{-2}}) = 22.30 \pm 0.14$ (Zafar et al. 2018a). This bump is the only unambiguous detection of such a feature in a GRB spectrum in more than a decade. Zafar et al. (2018a) derived a lower limit of [Zn/H] $\geqslant -0.98$ for the metallicity of the DLA.

Since our method is based on exploiting the observed extinction curves to constrain DLA metallicities, we first explain how we construct the extinction over wavelength from 912 Å to 1 cm. In the case of the GRB 180325A, for the wavelength range $3.3\ \mu{\rm m}^{-1} < \lambda^{-1} < 11\ \mu{\rm m}^{-1}$, we represent the extinction determined from the Fitzpatrick & Massa (1990) extinction law with the extinction parameters taken from Zafar et al. (2018a): $c_1 = -1.95\ \mu$m, $c_2 = 1.28$, $c_3 = 2.92$, $c_4 = 0.52$, $\gamma = 1.16\ \mu{\rm m}^{-1}$, $x_0 = 4.538\ \mu{\rm m}^{-1}$, $R_V = 4.58$, and $A_V = 1.58$. For the wavelength range $1.1\ \mu{\rm m}^{-1} < \lambda^{-1} < 3.3\ \mu{\rm m}^{-1}$, the extinction curve is defined by a cubic spline interpolation between a set of optical/IR anchor points and a pair of UV anchor points (Fitzpatrick & Massa 2007). For $0.9\ \mu{\rm m} < \lambda < 1$ cm, the extinction is approximated by the model extinction calculated from the standard silicate-graphite-PAH model of Wang et al. (2015). The final extinction curve is shown in Figure 1. For the ease of illustration, we only show in Figure 1 the extinction curve up to 100 μm.

In the case of the quasars, we employ the template-matching technique to measure the extinction, $A_{\rm V}$, and construct the extinction curve for the wavelength range $3.3\ \mu{\rm m}^{-1} < \lambda^{-1} < 11\ \mu{\rm m}^{-1}$ (Fitzpatrick & Massa 2007). Here, we iteratively redden the template quasar spectrum of Selsing et al. (2016) using the Small Magellanic Cloud (SMC) extinction curve (Gordon et al. 2003) until the reddened template spectrum best matches the observation (for more details see Fathivavsari 2020a). The results are shown in Figure 2. In this figure, the blue and red curves are the template quasar spectrum before and after applying the reddening, respectively. Moreover, for the wavelength ranges $1.1\ \mu{\rm m}^{-1} < \lambda^{-1} < 3.3\ \mu{\rm m}^{-1}$ and $0.9\ \mu{\rm m} < \lambda < 1$ cm, the extinction curve is approximated following the same approach as was employed to the GRB (see above).

3. Results

3.1. Metallicity Inferred from the Kramers–Kronig Relation

In this section, we employ the KK relation of Purcell (1969) to set a robust lower limit on the metallicity of the DLAs. For this purpose, we first define a grid of metallicities ranging from −2.0 to 0.0 with the step of 0.05 dex. For each metallicity in the grid, we calculate the area under the *expected* extinction curve. In practice, we calculate $V_{\rm dust}$/H and then use Equation (1) to convert it to the area under the extinction curve. The metallicity at which the expected area is equal to the observed one is taken as the lower limit of the metallicity. The areas under the observed extinction curves are listed in the 8th column of Table 1. Since these areas are calculated from the spectral range of 912 Å to 1 cm, they are considered as lower limits.

For the dust composition, we take into account three different compositions: (1) graphite and Fe-bearing silicates (

Table 1
Results of the KK Approach

ID	z_{em}	z_{abs}	N_{HI}	[X/H]	X	A_V	A_{int}	Z^1_{KK}	Z^2_{KK}	Z^3_{KK}	Ref.
J0112−0048	2.1485	2.1493	21.95 ± 0.10	-0.63 ± 0.15	Si II	0.37	11.6	$\geqslant -1.05$	$\geqslant -1.07$	$\geqslant -1.03$	(1)
J0823+0529	3.1875	3.1910	21.70 ± 0.10	-0.79 ± 0.10	Si II	0.14	8.1	$\geqslant -1.21$	$\geqslant -1.22$	$\geqslant -1.19$	(1)
J1142+0701	1.8700	1.8407	21.50 ± 0.15	-0.86 ± 0.20	Si II	0.13	12.2	$\geqslant -1.03$	$\geqslant -1.04$	$\geqslant -1.01$	(2)
J1154−0215	2.1810	2.1853	21.75 ± 0.10	-1.71 ± 0.20	Si II	0.07	3.6	$\geqslant -1.56$	$\geqslant -1.58$	$\geqslant -1.54$	(1)
J1155+0530	3.4800	3.3260	21.05 ± 0.10	-0.80 ± 0.11	S II	0.08	21.2	$\geqslant -0.79$	$\geqslant -0.81$	$\geqslant -0.77$	(2)
J1253+1007	3.0150	3.0312	21.30 ± 0.10	-1.45 ± 0.10	Si II	0.04	5.7	$\geqslant -1.36$	$\geqslant -1.37$	$\geqslant -1.34$	(1)
J1310+5424	1.9300	1.8006	21.45 ± 0.15	-0.52 ± 0.16	Si II	0.19	19.6	$\geqslant -0.82$	$\geqslant -0.84$	$\geqslant -0.80$	(2)
J1417+4132	2.0200	1.9509	21.85 ± 0.15	-0.93 ± 0.16	Zn II	0.19	7.5	$\geqslant -1.24$	$\geqslant -1.26$	$\geqslant -1.22$	(2)
J1509+1113	2.1100	2.0283	21.30 ± 0.15	-0.76 ± 0.16	S II	0.16	23.3	$\geqslant -0.75$	$\geqslant -0.77$	$\geqslant -0.73$	(2)
J1524+1030	2.0600	1.9409	21.65 ± 0.15	$\geqslant -0.72$	Zn II	0.35	22.0	$\geqslant -0.77$	$\geqslant -0.79$	$\geqslant -0.75$	(2)
J1552+1005	3.7220	3.6010	21.10 ± 0.10	-1.75 ± 0.11	S II	0.01	2.4	$\geqslant -1.74$	$\geqslant -1.75$	$\geqslant -1.71$	(3)
J1604+3951	3.1542	3.1633	21.75 ± 0.10	-1.19 ± 0.05	S II	0.06	3.0	$\geqslant -1.64$	$\geqslant -1.65$	$\geqslant -1.61$	(2)
J2100−0641	3.1295	3.0924	21.05 ± 0.15	-0.71 ± 0.16	S II	0.11	29.0	$\geqslant -0.65$	$\geqslant -0.67$	$\geqslant -0.63$	(2)
GRB 180325A	⋯	2.2486	22.30 ± 0.14	$\geqslant -0.98$	Zn II	1.58	32.1	$\geqslant -0.61$	$\geqslant -0.63$	$\geqslant -0.59$	(4)

Note. Column 1: the name of the quasar and/or GRB. Column 2: the emission redshift of the quasar. Column 3: the absorption redshift of the DLA. Column 4: logarithm of the neutral hydrogen column density of the DLA. Column 5: the observed metallicity of the DLA. Column 6: the low-ionization metal transition used in measuring the observed metallicity of the DLA. Column 7: the observed visual extinction. Column 8: the area under the observed extinction curve in unit of 10^{-27} mag cm^3 H^{-1}. Column 9: The KK lower limit of the metallicity by considering graphite and Fe-bearing silicates to be the main components of the dust. Column 10: the KK lower limit of the metallicity by considering graphite, Fe-lacking silicates, and iron oxides to be the main components of the dust. Column 11: the KK lower limit of the metallicity by considering graphite, Fe-lacking silicates, and pure iron to be the main components of the dust. Column 12: the references from which z_{em}, z_{abs}, N(H I), and [X/H] are compiled. Here (1), (2), (3), and (4) refer to Fathivavsari et al. (2016); Berg et al. (2015, 2016), and Zafar et al. (2018a), respectively.

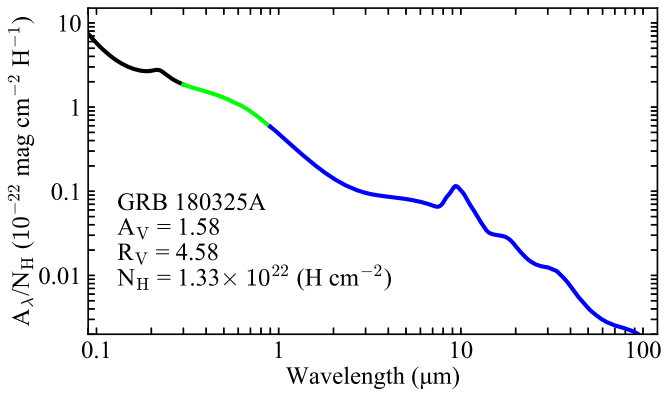

Figure 1. The extinction curve from the far-UV to the far-IR for GRB 180325A, with the Fitzpatrick & Massa (1990) curve for the $3.3\ \mu m^{-1} < \lambda^{-1} < 11\ \mu m^{-1}$ (black line), the Fitzpatrick & Massa (2007) curve for the $1.1\ \mu m^{-1} < \lambda^{-1} < 3.3\ \mu m^{-1}$ (green line), and the Wang et al. (2015) curve for the $\lambda > 0.9\ \mu m$ (blue line).

i.e., olivine $MgFeSiO_4$). For this composition, the term $F\,V_{dust}/H$ in Equation (1) is defined as

$$F\,\frac{V_{dust}}{H} = F_{gra}\,\frac{V_{gra}}{H} + F_{sil}\,\frac{V_{sil}}{H}. \quad (3)$$

(2) graphite, Fe-lacking silicates (i.e., enstatite $MgSiO_3$), and pure iron (Poteet et al. 2015; Dwek 2016). Here, the term $F\,V_{dust}/H$ is defined as

$$F\,\frac{V_{dust}}{H} = F_{gra}\,\frac{V_{gra}}{H} + F_{sil}\,\frac{V_{sil}}{H} + F_{Fe}\,\frac{V_{Fe}}{H}. \quad (4)$$

(3) graphite, Fe-lacking silicates, and iron oxides (i.e., FeO, Fe_2O_3, and Fe_3O_4). For this composition, the term $F\,V_{dust}/H$ is defined as

$$F\,\frac{V_{dust}}{H} = F_{gra}\,\frac{V_{gra}}{H} + F_{sil}\,\frac{V_{sil}}{H} + F^{oxide}_{Fe}\,\frac{V^{oxide}_{Fe}}{H}, \quad (5)$$

where

$$F^{oxide}_{Fe}\,\frac{V^{oxide}_{Fe}}{H} = F_{FeO}\,\frac{V_{FeO}}{H} + F_{Fe_2O_3}\,\frac{V_{Fe_2O_3}}{H} + F_{Fe_3O_4}\,\frac{V_{Fe_3O_4}}{H} \quad (6)$$

Here, we assume that all Si and Fe atoms, and 70 percent of carbon atoms, are locked up in dust. For the iron oxides, we also assume that Fe atoms are equally shared among the three different iron oxides (Zuo et al. 2020). The F factors for graphite, silicates, iron, and iron oxides are listed in Table 8 of Zuo et al. (2020).

Table 1 summarizes the results of our KK approach. For better visualization of the results, we also plot in Figure 3 the observed (i.e., [X/H]) and the KK lower limit (i.e., Z_{KK}) metallicities of the DLAs. As shown in this figure, we achieve $Z_{KK} \leqslant$ [X/H] for all DLAs along the quasar lines of sight, within the uncertainty of the observed metallicities. For the GRB line of sight, our new lower limit is ∼0.4 dex higher than the one reported by Zafar et al. (2018a). This implies that the DLA along the GRB 180325A sightline could have a metallicity even higher than ∼−0.6.

3.2. Metallicity Inferred from Modeling the Observed Extinction Curve

As mentioned before, the GRB extinction curve exhibits a strong 2175 Å extinction bump, which is a common characteristic feature of Galactic sightlines. In this section, we try to estimate some lower limits for the metallicity of the DLA detected along the GRB line of sight by modeling the GRB extinction curve. For this purpose, we consider two kinds of dust models: (1) the two-component model of Mathis et al. (1977) and (2) the three-component model of Compiègne et al. (2011).

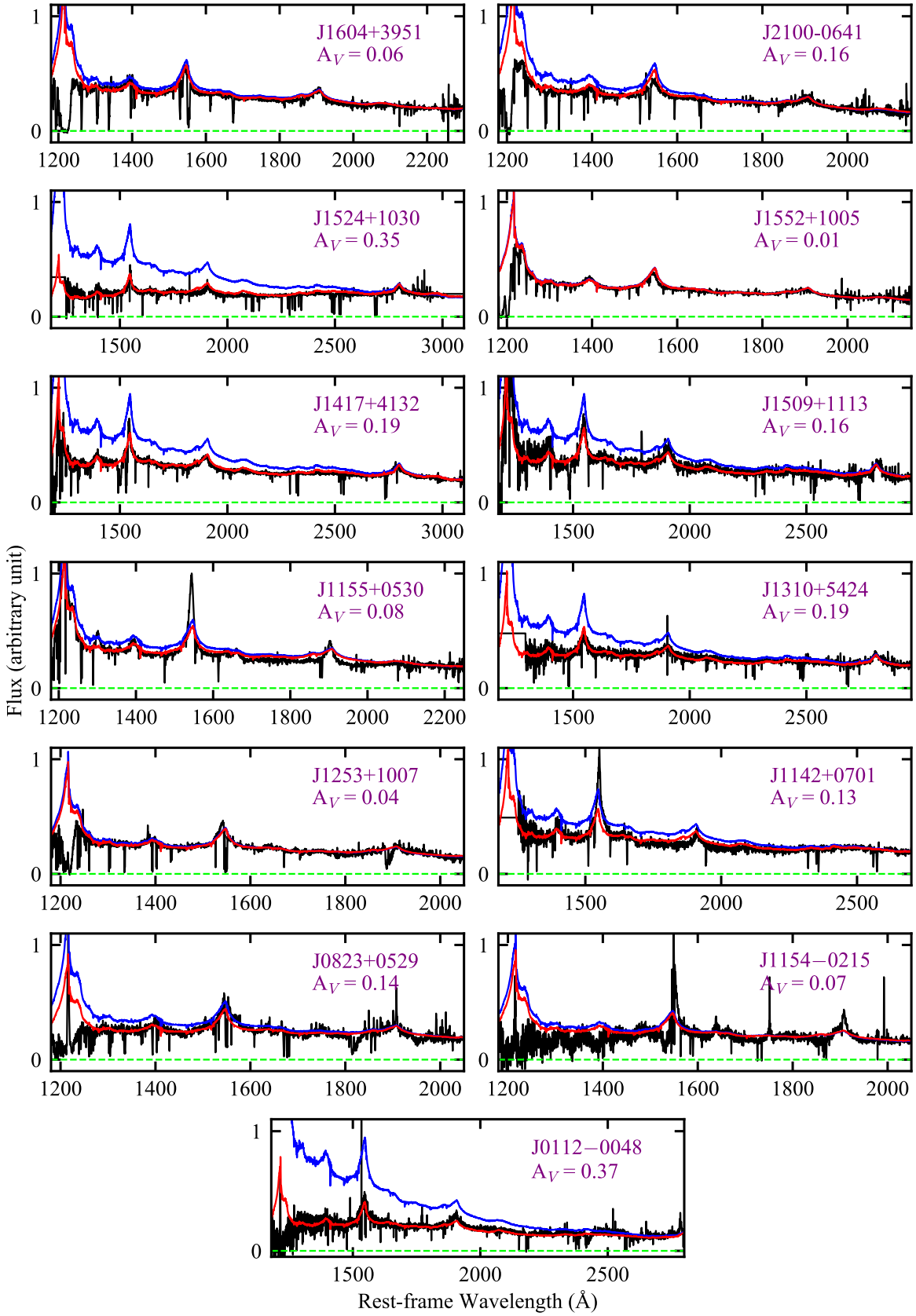

Figure 2. Spectra of quasars in our sample. In each panel, the blue curve shows the quasar template spectrum of Selsing et al. (2016), and the red curve shows the same quasar template spectrum but reddened by the SMC extinction law.

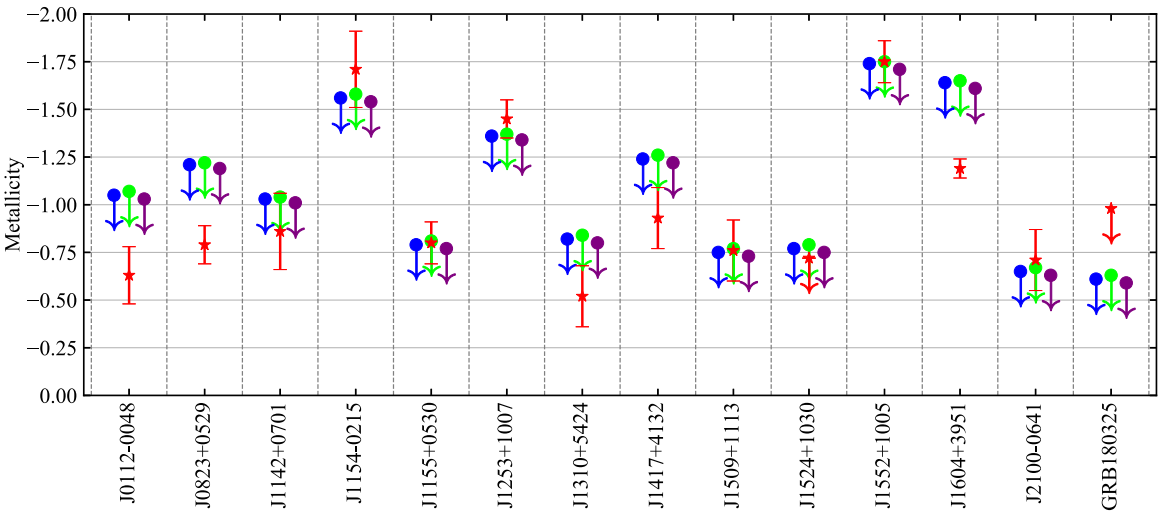

Figure 3. Visual representation of the observed and the KK approach metallicities. Here, the red symbols are the observed data points, and the blue, green, and purple symbols represent the lower limits from the KK approach.

3.2.1. Two-component Dust Model

In this section, we model the observed extinction curve using an extinction model with two dust components: amorphous silicate and graphite (Mathis et al. 1977; Draine & Lee 1984; Weingartner & Draine 2001; Wang et al. 2015). Here, we show that the adopted metallicity is very important in reproducing the observed extinction curve. This would allow us to put a constraint on the metallicity of the DLA. Similar to Mishra & Li (2015, 2017), an exponentially cut-off power-law size distribution is adopted for both dust components:

$$\frac{1}{n_{\rm H}}\frac{dn_i}{da} = B_i a^{-\alpha_i}\exp(-a/a_{c,i}). \quad (7)$$

Here, a is the radius of the dust particles, which is in the range of 50 Å $< a <$ 2.5 μm. The dust particles are assumed to be spherical so that the Mie theory can be used to compute extinction cross sections (Mathis et al. 1977). The term $n_{\rm H}$ is the number density of hydrogen nuclei, dn_i is the number density of each type of dust ("i" represents either silicate or graphite) with radii between a and $a + da$, α_i and $a_{c,i}$ are, respectively, the power-law index and exponential cut-off size, and B_i relates to the total amount of each dust type present in the cloud.

The total extinction per hydrogen column at wavelength λ is given by

$$A_\lambda/N_{\rm H} = 1.086\sum_i \int da \frac{1}{n_{\rm H}}\frac{dn_i}{da}C_{{\rm ext},i}(a,\lambda), \quad (8)$$

where the summation is over the silicate and graphite dust grains, $N_{\rm H}$ is the hydrogen column density, and $C_{{\rm ext},i}(a, \lambda)$ is the extinction cross section of dust grains of size a at wavelength λ. For each silicate and graphite dust grain, $C_{{\rm ext},i}(a, \lambda)$ can be calculated from the Mie theory by using the dielectric functions of "astronomical" silicate and graphite from Draine & Lee (1984).

We use the Levenberg–Marquardt method (Press et al. 1992) to fit the observed extinction curve from 0.1 $\mu{\rm m}^{-1}$ to 8 $\mu{\rm m}^{-1}$. We evaluate the extinction at 100 wavelengths, equally spaced in ln λ, and minimize $\chi^2 = \chi_1^2 + \chi_2^2$, which is the sum of two error functions:

$$\chi_1^2 = \sum_i \frac{[A_{\rm obs}(\lambda_i)/10^{21} - A_{\rm mod}(\lambda_i)/10^{21}]^2}{\sigma_i^2}, \quad (9)$$

and

$$\chi_2^2 = 0.4[\max(\tilde{\rm C}, 1) - 1]^{1.5} + 0.4[\max(\tilde{\rm Si}, 1) - 1]^{1.5}, \quad (10)$$

where $A_{\rm obs}(\lambda_i)$ is the observed extinction, $A_{\rm mod}(\lambda_i)$ is the extinction computed by the model, σ_i is the weight, $\tilde{\rm C} = [{\rm C/H}]_{\rm dust}/[{\rm C/H}]_{\rm DLA}$, and $\tilde{\rm Si} = [{\rm Si/H}]_{\rm dust}/[{\rm Si/H}]_{\rm DLA}$. Here, $[{\rm C/H}]_{\rm DLA}$ and $[{\rm Si/H}]_{\rm DLA}$ represent the number of C and Si atoms relative to hydrogen for each adopted metallicity. $[{\rm C/H}]_{\rm dust}$ and $[{\rm Si/H}]_{\rm dust}$ are calculated using the following equations:

$$[{\rm C/H}]_{\rm dust} = (B_{\rm C}/\mu_{\rm C}\, m_{\rm H}) \times \int da(4\pi/3)a^3\rho_{\rm gra}a^{-\alpha_{\rm C}}\exp(-a/a_{c,{\rm C}}) \quad (11)$$

$$[{\rm Si/H}]_{\rm dust} = (B_{\rm S}/\mu_{\rm sil}\, m_{\rm H}) \times \int da(4\pi/3)a^3\rho_{\rm sil}a^{-\alpha_{\rm S}}\exp(-a/a_{c,{\rm S}}), \quad (12)$$

where $\mu_{\rm C}$ (=12) is the atomic weight of carbon, $\mu_{\rm sil}$ (=172) is the atomic weight of silicate grains with the stoichiometric composition of $MgFeSiO_4$, $\rho_{\rm gra}$ is the mass density of graphite, and $B_{\rm C}$ and $B_{\rm S}$ are, respectively, related to the total amount of graphite and silicate present in the cloud. We take $\sigma_i = 1\,\sigma_{\rm obs}$ for 2 $\mu{\rm m}^{-1} < \lambda^{-1} < 8\ \mu{\rm m}^{-1}$ and $\sigma_i = 5\,\sigma_{\rm obs}$ for $\lambda^{-1} < 2\ \mu{\rm m}^{-1}$ since the observed extinction in the infrared region is uncertain. Here, $\sigma_{\rm obs} = 0.1$ is the standard deviation of the observed data points estimated from the mean signal-to-noise ratio (SNR) of the observed spectrum (i.e., SNR $\sim$ 5). The term χ_2^2 in Equation (10) is a *penalty* which keeps the model-consumed C and Si abundances from grossly exceeding the maximum values allowed by the assumed metallicity.

Similar to the previous section, we assume that all Si and 70 percent of C atoms are locked up in dust grains. We then fit the observed extinction curve and reach $\chi^2 = 1.5$ for the

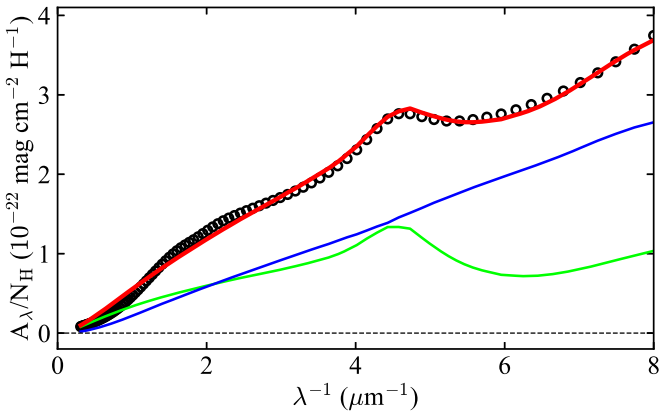

Figure 4. Observed (black circles) and model (red line) extinction curves of GRB 180325A for the two-component dust model. The red line is the combination of the contributions from the silicate (blue line) and graphite (green line) dust grains.

metallicity of $Z \sim -0.45$. Figure 4 shows the resulting fit, and Table 2 lists the parameters of the fit. In Figure 4, the black circles show the observed extinction curve and the red curve shows the model extinction curve, which is the combination of silicate (blue curve) and graphite (green curve) contributions. We also checked the effect of increasing N^{C}_{dust}/N^{C}_{tot} and found that this would lead to a slightly lower metallicity, i.e., $-0.45 < Z < -0.50$, but with higher χ^2 ($\sim$2.6). Moreover, we also found that a smaller N^{C}_{dust}/N^{C}_{tot} ratio would result in a slightly higher metallicity ($Z \sim -0.40$).

3.2.2. Three-component Dust Model

In this section, we try to model the GRB extinction curve using a model with three dust components: (i) PAHs, (ii) hydrogenated amorphous carbon (amC), and (iii) amorphous silicates (aSil). Here, the population of amorphous carbon dust is divided into small (SamC) and large (LamC) grains, but with a continuous overall PAH + amC size distribution (see Figure 1 in Compiègne et al. 2011). The PAH and SamC size distributions are assumed to be log-normal with a_0 and σ representing the center radius and the width of the distribution, respectively. Moreover, the LamC and aSil size distributions have a power-law form (i.e., a^{α}) starting with the minimum size of a_{min} and an exponential cut-off of the following form

$$\begin{cases} \exp(-[(a - a_t)/a_c]^{\gamma}) & a \geqslant a_t \\ 1 & a < a_t. \end{cases} \quad (13)$$

Here, our goal is to find the metallicity for which the model extinction curve best matches the observation. For this purpose, we first define a grid of metallicities ranging from -1.0 (i.e., the lower limit reported by Zafar et al. 2018a) to 0.0 with the step of 0.1 dex. Then, for each metallicity in the grid, we adjust the size distribution of the different dust populations until the minimum χ^2 is reached. The χ^2 is defined as in Equation (9). The model extinction, A_{mod}, is calculated using the `DustEM` code, which is freely available online.[1] Similar to Section 3.2.1, we take $\sigma_i = 5\,\sigma_{obs}$ for $\lambda^{-1} < 2\,\mu m^{-1}$ and $\sigma_i = 1\,\sigma_{obs}$ for $2\,\mu m^{-1} < \lambda^{-1} < 8\,\mu m^{-1}$ since the observed extinction in the infrared region is uncertain. Figure 5 shows the minimum χ^2 value for each metallicity in the grid. The χ^2 for $Z = -1.0$, -0.9, and 0.0 are very large, therefore, for the ease of illustration, they are not shown in Figure 5. As shown here, the best match between the model and the observed extinction curve occurs at $Z = -0.5$. Figure 6 shows the best fit to the observed extinction curve, which is reached for $Z = -0.5$. Table 3 lists the parameters of the fit.

[1] https://www.ias.u-psud.fr/DUSTEM/dustem_code.html

Table 2
Best Model Parameters for Fitting the GRB Extinction Curve with a Two-component Dust Model

ID	α_i	$a_{c,i}(\mu m)$	B_i
Silicate	3.21	0.22	14.0×10^{-25}
Graphite	3.27	0.37	2.6×10^{-25}

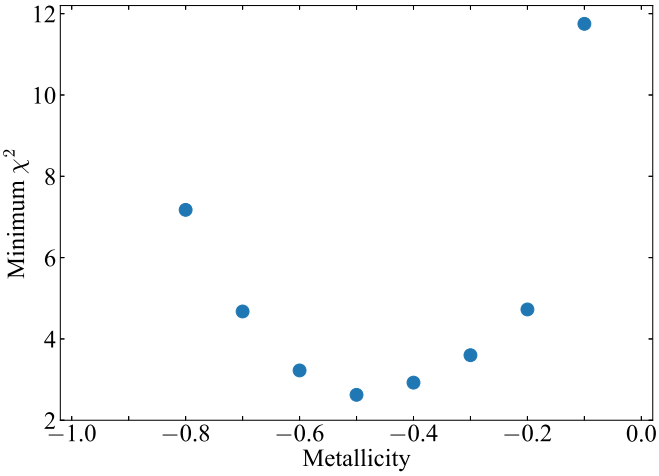

Figure 5. Minimum χ^2 as function of metallicity for the three-component dust model (see the text).

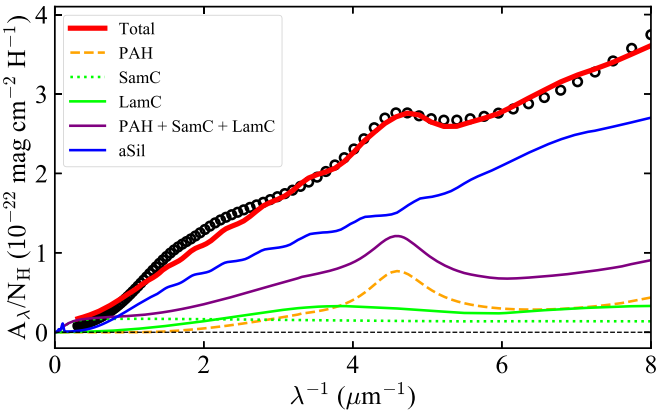

Figure 6. Observed (black circles) and model (red line) extinction curves of GRB 180325A for the three-component dust model. The other colored curves show the contributions from different dust components.

4. Summary and Conclusion

In this work, we presented a method to constrain the metallicities of high-redshift (i.e., $z_{abs} \geqslant 1.8$) DLA absorbers using the observed extinction curves. We used the observed extinction curves of 13 quasars and one GRB in order to demonstrate the method. This is the first time the extinction curve is exploited to constrain the metallicities of extragalactic absorbers. We used the KK relation, which is a model-independent approach, to put some lower limits on the metallicities of the DLAs detected in the spectra of the quasars and the GRB. Here, the lower limits are calculated for three

Table 3
Parameters of the Fit for Our Best Dust Model

	σ	a_0 (nm)			(M/M_H)
PAH	0.16	0.9			7.9×10^{-5}
SamC	1.26	10			8.3×10^{-5}
	α	a_{min} (nm)	(a_c, a_t) (nm)	γ	
LamC	−1.72	4.0	(880, 70)	1.72	5.59×10^{-4}
aSil	−3.43	4.0	(280, 120)	1.23	17.6×10^{-4}

Note. The last column is the mass abundance per hydrogen for each dust component.

different dust compositions: (1) graphite and Fe-bearing silicates, (2) graphite, Fe-lacking silicates, and pure iron, and (3) graphite, Fe-lacking silicates, and iron oxides. Interestingly, the results from the different dust compositions are consistent both with each other and with the observations.

The GRB extinction curve exhibits a very strong 2175 Å extinction bump. We therefore tried to model the GRB extinction curve using dust models with two (i.e., graphite and silicates) and three (i.e., PAH, hydrogenated amorphous carbon, and silicates) dust components. The two-component model results in a metallicity of $Z \sim -0.45$, while the three-component model gives $Z \sim -0.50$. That said, the lower limit from the KK approach for this DLA is $Z \geqslant -0.60$. Since the KK approach is model-independent, we propose ~ -0.6 as the new lower limit for the metallicity of the DLA detected along the line of sight to GRB 180325A. Modeling a large sample of extinction curves with the 2175 Å extinction bump and measured DLA metallicities would allow a thorough comparison between the KK and the model-dependent approach.

When the precise measurement of the metallicity of a DLA is not possible (e.g., due to the saturation of important absorption lines such as Zn II), the techniques employed in this paper can be used to constrain the metallicity, especially in absorbers associated with GRBs (due to their simple spectral energy distributions which follow a power-law relation and lack prominent emission lines) and quasar absorbers with $z_{abs} \sim z_{em}$, such as eclipsing and ghostly DLAs. Since the presence of quasar broad emission lines could complicate the process of extracting the extinction curve from the quasar spectrum, these complications are at minimum when $z_{abs} \sim z_{em}$, hence this technique could be better suited for such absorbers.

The author would like to thank the referee for useful comments that improved the quality of the paper. The author would also like to thank Prof. Aigen Li and Dr. Tayyaba Zafar for useful discussions.

ORCID iDs

Hassan Fathivavsari https://orcid.org/0000-0002-1840-8157

References

Adamson, A. J., Whittet, D. C. B., & Duley, W. W. 1990, MNRAS, 243, 400
Allamandola, L. J., Tielens, A. G. G. M., & Barker, J. R. 1985, ApJL, 290, L25
Anders, E., & Grevesse, N. 1989, GeCoA, 53, 197
Asplund, M., Grevesse, N., Sauval, A. J., & Scott, P. 2009, ARA&A, 47, 481
Bekki, K., Hirashita, H., & Tsujimoto, T. 2015, ApJ, 810, 39
Berg, T. A. M., Ellison, S. L., Sánchez-Ramírez, R., et al. 2016, MNRAS, 463, 3021
Berg, T. A. M., Neeleman, M., Prochaska, J. X., Ellison, S. L., & Wolfe, A. M. 2015, PASP, 127, 167
Compiègne, M., Verstraete, L., Jones, A., et al. 2011, A&A, 525, A103
De Cia, A., Ledoux, C., Savaglio, S., Schady, P., & Vreeswijk, P. M. 2013, A&A, 560, A88
Draine, B. T., & Lee, H. M. 1984, ApJ, 285, 89
Draine, B. T., & Malhotra, S. 1993, ApJ, 414, 632
Dwek, E. 2016, ApJ, 825, 136
Fathivavsari, H. 2020a, ApJ, 888, 85
Fathivavsari, H. 2020b, ApJ, 901, 123
Fathivavsari, H., Petitjean, P., Jamialahmadi, N., et al. 2018, MNRAS, 477, 5625
Fathivavsari, H., Petitjean, P., Noterdaeme, P., et al. 2015, MNRAS, 454, 876
Fathivavsari, H., Petitjean, P., Noterdaeme, P., et al. 2016, MNRAS, 461, 1816
Fathivavsari, H., Petitjean, P., Zou, S., et al. 2017, MNRAS, 466, L58
Fitzpatrick, E. L., & Massa, D. 1990, ApJS, 72, 163
Fitzpatrick, E. L., & Massa, D. 2007, ApJ, 663, 320
Gao, W., Zhao, R., Gao, J., Jiang, B., & Li, J. 2020, P&SS, 183, 104627
Gordon, K. D., Clayton, G. C., Misselt, K. A., Landolt, A. U., & Wolff, M. J. 2003, ApJ, 594, 279
Gudennavar, S. B., Bubbly, S. G., Preethi, K., & Murthy, J. 2012, ApJS, 199, 8
Henning, T. 2010, ARA&A, 48, 21
Jaeger, C., Mutschke, H., Begemann, B., Dorschner, J., & Henning, T. 1994, A&A, 292, 641
Kemper, F., Vriend, W. J., & Tielens, A. G. G. M. 2004, ApJ, 609, 826
Kim, S.-H., Martin, P. G., & Hendry, P. D. 1994, ApJ, 422, 164
Laor, A., & Draine, B. T. 1993, ApJ, 402, 441
Leger, A., & Puget, J. L. 1984, A&A, 500, 279
Li, A. 2005, ApJ, 622, 965
Li, A., & Draine, B. T. 2001a, ApJL, 550, L213
Li, A., & Draine, B. T. 2001b, ApJ, 554, 778
Li, A., Liang, S. L., Kann, D. A., et al. 2008, ApJ, 685, 1046
Liang, S. L., & Li, A. 2009, ApJL, 690, L56
Liang, S. L., & Li, A. 2010, ApJ, 710, 648
Ma, X.-Y., Zhu, Y.-Y., Yan, Q.-B., You, J.-Y., & Su, G. 2020, MNRAS, 497, 2190
Mathis, J. S., Rumpl, W., & Nordsieck, K. H. 1977, ApJ, 217, 425
Mishra, A., & Li, A. 2015, ApJ, 809, 120
Mishra, A., & Li, A. 2017, ApJ, 850, 138
Mulas, G., Zonca, A., Casu, S., & Cecchi-Pestellini, C. 2013, ApJS, 207, 7
Papoular, R. J., & Papoular, R. 2009, MNRAS, 394, 2175
Pendleton, Y. J., & Allamandola, L. J. 2002, ApJS, 138, 75
Poteet, C. A., Whittet, D. C. B., & Draine, B. T. 2015, ApJ, 801, 110
Press, W. H., Teukolsky, S. A., Vetterling, W. T., & Flannery, B. P. 1992, Numerical Recipes in FORTRAN. The Art of Scientific Computing (Cambridge: Cambridge Univ. Press)
Purcell, E. M. 1969, ApJ, 158, 433
Savage, B. D., Cardelli, J. A., & Sofia, U. J. 1992, ApJ, 401, 706
Selsing, J., Fynbo, J. P. U., Christensen, L., & Krogager, J.-K. 2016, A&A, 585, A87
Sofia, U. J., Cardelli, J. A., & Savage, B. D. 1994, ApJ, 430, 650
Spitzer, L., Jr., & Jenkins, E. B. 1975, ARA&A, 13, 133
Spitzer, L., Jr., & Fitzpatrick, E. L. 1995, ApJ, 445, 196
Stecher, T. P., & Donn, B. 1965, ApJ, 142, 1681
Steglich, M., Jäger, C., Rouillé, G., et al. 2010, ApJL, 712, L16
Vladilo, G. 1998, ApJ, 493, 583
Voshchinnikov, N. V., & Henning, T. 2010, A&A, 517, A45
Wang, S., Li, A., & Jiang, B. W. 2015, ApJ, 811, 38
Weingartner, J. C., & Draine, B. T. 2001, ApJ, 548, 296
Welty, D. E., Lauroesch, J. T., Blades, J. C., Hobbs, L. M., & York, D. G. 1997, ApJ, 489, 672
Xiang, F. Y., Li, A., & Zhong, J. X. 2011, ApJ, 733, 91
Zafar, T., Heintz, K. E., Fynbo, J. P. U., et al. 2018a, ApJL, 860, L21
Zafar, T., Watson, D., Elíasdóttir, Á., et al. 2012, ApJ, 753, 82
Zafar, T., Watson, D., Fynbo, J. P. U., et al. 2011, A&A, 532, A143
Zafar, T., Watson, D., Møller, P., et al. 2018b, MNRAS, 479, 1542
Zonca, A., Cecchi-Pestellini, C., Mulas, G., & Malloci, G. 2011, MNRAS, 410, 1932
Zuo, W. B., Li, A., & Zhao, G. 2021, ApJS, 252, 22